

Nematic quantum disordered state in FeSe

Ruixian Liu,¹ Matthew B. Stone,² Shang Gao,² Mitsutaka Nakamura,³ Kazuya Kamazawa,⁴ Aleksandra Krajewska,⁵ Helen C. Walker,⁵ Peng Cheng,⁶ Rong Yu,⁶ Qimiao Si,⁷ Pengcheng Dai,^{7,*} and Xingye Lu^{1,†}

¹*Center for Advanced Quantum Studies and Department of Physics, Beijing Normal University, Beijing 100875, China*

²*Neutron Scattering Division, Oak Ridge National Laboratory, Oak Ridge, Tennessee 37831, USA*

³*J-PARC Center, Japan Atomic Energy Agency (JAEA), Tokai, Ibaraki 319-1195, Japan*

⁴*Research Center for Neutron Science and Technology,*

Comprehensive Research Organization for Science and Society, Tokai, Ibaraki 319-1106, Japan

⁵*ISIS Facility, Rutherford Appleton Laboratory, STFC, Chilton, Didcot OX11 0QX, United Kingdom*

⁶*Department of Physics, Renmin University of China, Beijing 100872, China*

⁷*Department of Physics and Astronomy, Rice Center for Quantum Materials, Rice University, Houston, TX 77005, USA*

(Dated: April 3, 2025)

The unusual quantum-disordered magnetic ground state intertwined with superconductivity and electronic nematicity in FeSe has been a research focus in iron-based superconductors. However, the intrinsic spin excitations across the entire Brillouin zone in detwinned FeSe, which forms the basis for a microscopic understanding of the magnetic state and superconductivity, remain to be determined. Here, we use inelastic neutron scattering to map out the spin excitations of FeSe detwinned with a uniaxial-strain device. We find that the stripe spin excitations ($\mathbf{Q}=(1, 0)/(0, 1)$) exhibit the C_2 symmetry up to $E \approx 120$ meV, while the Néel spin excitations ($\mathbf{Q}=(1, 1)$) retain their C_4 symmetry in the nematic state. The temperature dependence of the difference in the spin excitations at $\mathbf{Q}=(1, 0)$ and $(0, 1)$ for temperatures above the structural phase transition unambiguously shows the establishment of the nematic quantum disordered state. The similarity of the Néel excitations in FeSe and NaFeAs suggests that the Néel excitations are driven by the enhanced electron correlations in the $3d_{xy}$ orbital. By determining the key features of the stripe excitations and fitting their dispersions using a Heisenberg Hamiltonian with biquadratic interaction (J_1 - K - J_2), we establish a spin-interaction phase diagram and conclude that FeSe is close to a crossover region between the antiferroquadrupolar, Néel, and stripe ordering regimes. The results provide an experimental basis for establishing a microscopic theoretical model to describe the origin and intertwining of the emergent orders in iron-based superconductors.

The parent compounds of iron pnictide superconductors exhibit a tetragonal-to-orthorhombic structural phase transition at T_s and then form collinear long-range antiferromagnetic (AF) stripe order at the wave vector $\mathbf{Q}_{AF} = (1, 0)$ below T_N ($T_N \leq T_s$) [1, 2]. At temperatures below T_s , iron pnictides establish an electronic nematic phase where the electronic and magnetic properties along the $\mathbf{Q} = (1, 0)$ direction are different from those along the $(0, 1)$ direction [3–13]. With increasing electron or hole doping, both T_N and T_s decrease and vanish near optimal superconductivity but AF and nematic fluctuations remain, thus suggesting their important role for superconductivity [2, 3, 6, 7]. While most iron-based superconductors follow this paradigm, iron chalcogenide FeSe is different [14]. With a simple layered structure, the stoichiometric FeSe undergoes a tetragonal-to-orthorhombic structural (nematic) transition at $T_s = 90$ K, and then becomes superconducting at $T_c \approx 8$ K without static AF order (Fig. 1(a)) [15–18]. Since nematic phase transitions for iron pnictides and FeSe occur below room temperature with small orthorhombic lattice distortions, samples are twinned below T_s where the $(1, 0)$ and $(0, 1)$ directions are mixed and cannot be separated in most spectroscopic measurements [9, 12]. While inelastic neutron scattering (INS) experiments on twinned iron pnictides such as BaFe_2As_2 have spin excitations stemming from the stripe ordering $\mathbf{Q}_{AF} = (1, 0)/(0, 1)$ positions consistent with expectations [19], similar measurements on twinned FeSe reveal spin excitations at the stripe ($\mathbf{Q}_{AF} = (1, 0)/(0, 1)$) and Néel ($\mathbf{Q}_N = (1, 1)$) ordering wave vectors [20]. The absence

of static AF order in FeSe was interpreted as arising from the magnetic frustration due to competing stripe and Néel interactions [21–23].

As the broad spin excitations centered around $\mathbf{Q}_N = (1, 1)$ merge with those stemming from $\mathbf{Q}_{AF} = (1, 0)/(0, 1)$ for $E \gtrsim 70$ meV in a twinned sample [20], it is unclear how to untangle the intrinsic spin excitations of FeSe from those due to twin domains. To understand the unusual magnetic state of FeSe, it is therefore imperative to map out its spin excitations in a twin-free sample. In previous work, we have carried out INS experiments on partially detwinned FeSe by gluing them on uniaxial strained BaFe_2As_2 substrates [13, 24]. However, spin waves from the BaFe_2As_2 substrates overwhelm the magnetic signal from FeSe for spin excitation energies $E \gtrsim 10$ meV and temperature across T_s [24]. Resonant inelastic X-ray scattering (RIXS) experiments on the FeSe crystal detwinned by the same method are capable of avoiding the substrate spin waves. These measurements unveil a large spin excitation anisotropy up to energy of $E \sim 200$ meV below T_s [25]; however, the limited momentum transfer of the Fe L_3 RIXS ($|\mathbf{q}_\parallel| \lesssim 0.5 \frac{2\pi}{a_o}$) means that one cannot access \mathbf{Q}_{AF} and \mathbf{Q}_N positions in these measurements.

In this work, we use INS to map out the energy-momentum dispersion of intrinsic spin excitations of FeSe, enabled by a newly designed low-background uniaxial-strain detwining device (Fig. 1(b)) [26], across the entire Brillouin zone (BZ). Our results identified the symmetries of the stripe and the Néel spin excitations (Figs. 1(c) and 1(d)), as well as

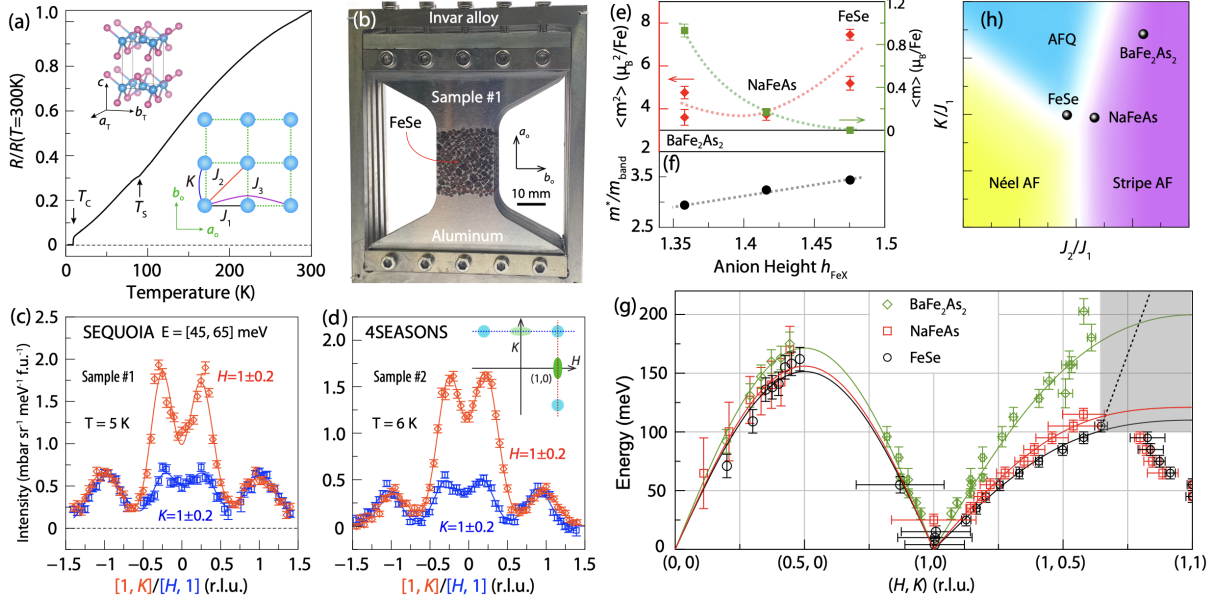


FIG. 1: Sample characterization, detwinning device and summary of the key results. (a) Temperature-dependent resistivity of FeSe single crystal. The left-upper inset illustrates the crystal structure of FeSe in tetragonal notation; the right-lower inset shows the orthorhombic unit cell in the Fe plane. J_1 , J_2 , and J_3 represent the nearest-neighbor (NN), next-NN, and next-next-NN exchange interactions between Fe ions. K denotes the biquadratic interaction between the adjacent Fe ions. (b) The uniaxial-strain device based on the differential thermal expansion coefficients between the Invar alloy ($\text{Fe}_{0.64}\text{Ni}_{0.36}$) frame and the aluminum sheet. (c), (d) One-dimensional constant-energy cuts ($E = 55 \pm 10$ meV) of the spin excitations along $[1, K]$ and $[H, 1]$ directions collected at the SEQUOIA (c) and 4SEASONS (d) time-of-flight spectrometers using incident energy of 147.5 meV and 80 meV, respectively. The inset of (d) depicts the positions of the stripe and Néel spin excitations in $[H, K]$ space, and the trajectories (blue and red dashed lines with arrowheads) for the 1D cuts shown in (c) and (d). (e), (f) Static (green squares) and fluctuating (red diamonds) magnetic moment (f), and the electron correlation (m^*/m_{band}) at the $3d_{xy}$ orbital (f) as a function of the anion height h_{FeX} . The data points in (f) are from ref. [27]. (g) Spin-excitation dispersions for BaFe_2As_2 (green diamonds), NaFeAs (red squares), and FeSe (black circles). The data points in the range $(0, 0)$ - $(0.5, 0)$ were measured with RIXS [25, 28]. The data points for BaFe_2As_2 and NaFeAs obtained with INS are extracted from refs. [13, 29]. The green, red, and black solid curves are the fittings of the dispersions with the J_1 - K - J_2 model. The gray-shaded area marks the (\mathbf{Q}, E) region where the spin excitations are heavily damped. The black dashed line schematically shows that the spin-excitation dispersion turns up and deviates from the fitting. (h) The ratios K/J_1 and J_2/J_1 for the fittings of the dispersions for BaFe_2As_2 (ref. [13]), NaFeAs (ref. [29]), and FeSe . The INS data of BaFe_2As_2 , NaFeAs , and FeSe were collected at $T = 7$ K, 5 K, and 5 K, respectively.

their energy-momentum dispersions and the temperature dependence across the nematic phase transition. By analyzing the features of the spin excitations in FeSe, NaFeAs, and BaFe_2As_2 , we find that the Néel excitations are somewhat independent of the stripe excitations and should be driven by the enhanced electron correlations of the d_{xy} orbital (Fig. 1(e)-(f)). Through fitting the stripe-excitation dispersions using a Heisenberg Hamiltonian with biquadratic interaction (J_1 - K - J_2) [30, 31], we establish a spin-interaction phase diagram for FeSe, NaFeAs and BaFe_2As_2 . As the low-energy stripe excitations in FeSe exhibit a linear-in-energy spectral weight and nematic spin correlations that can be described in an antiferroquadrupolar (AFQ) ordering regime [22, 32], we argue that FeSe is positioned close to a crossover regime where the AFQ, Néel, and stripe orders intersect [26]. The results provide an experimental basis for establishing a microscopic theoretical model to describe the origin and the intertwining of the emergent orders in iron-based superconductors (Figs. 1(f)-1(h)).

Uniaxial-strain device to detwin a large amount of FeSe single crystals

We describe in Fig. 1(a)-(d) the characterization of the sample and the detwinning efficiency of the uniaxial-strain device. Figure 1(a) shows the resistivity of FeSe as a function of temperature. The two clear features on the resistivity curve (marked by black arrows) correspond to the nematic and the superconducting transitions at $T_s = 90$ K and $T_c = 8.5$ K, respectively. Figure 1(b) displays a photo of Sample #1 for the INS experiment, which consists of five separate uniaxial-strain devices stacked along the c -axis containing ~ 1500 pieces (~ 1.61 grams) of thin FeSe crystals co-aligned along the tetragonal $[1, 1, 0]$ direction. The FeSe crystals are attached to 0.2 mm thick aluminum alloy (6061) sheets using type-M CYTOP. The uniaxial-strain device is designed based on the differential thermal expansion coefficients between the Invar alloy ($\alpha \approx -2 \times 10^{-6}/\text{K}$) outer frame and the aluminum ($\alpha \approx -24 \times 10^{-6}/\text{K}$) sheet fixed on the frame. While cooling, the thermal expansion difference

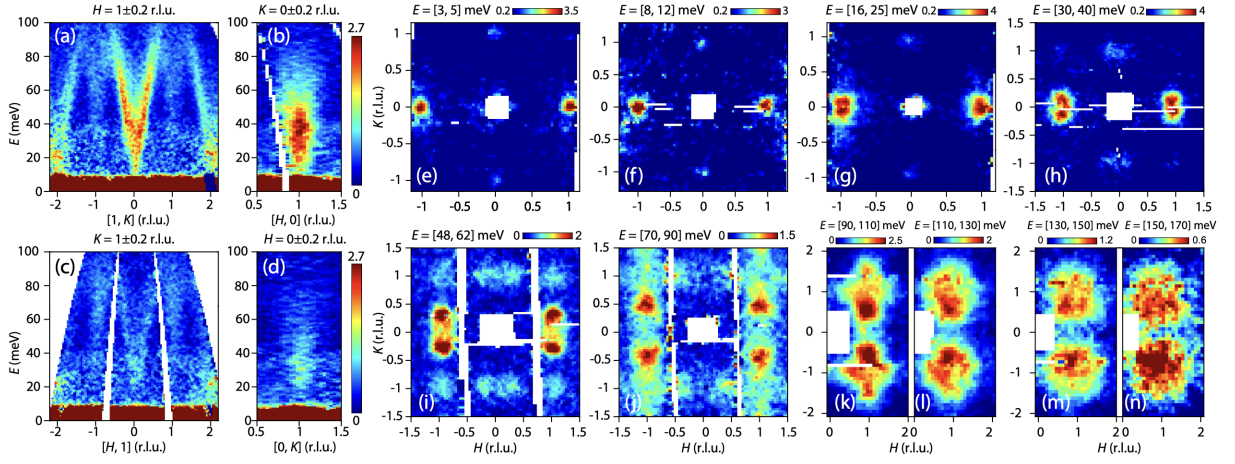


FIG. 2: **Two-dimensional slices of the magnetic excitations in detwinned FeSe.** (a)-(d) Energy-vs-momentum slices of the magnetic excitations across $\mathbf{Q} = (1, 0)$, $(0, 1)$ and $(1, 1)$ measured with $E_i = 147.5$ meV at $T = 5$ K. (e-n) Constant-energy slices of the magnetic excitations, with $E_i = 21$ meV (e), 36 meV (f)-(g), 80 meV (h), 147.5 meV (i)-(j), and 295 meV (k)-(n) at based temperatures. For the $E_i = 147.5$ meV data ((a)-(d), and (i)-(j)), the scattering signal of an empty strain device with CYTOP has been subtracted as a background. A $|\mathbf{Q}|$ -dependent background has been subtracted from the data shown in (e)-(h) [20], and energy-dependent flat backgrounds are subtracted from the data (k)-(n).

between the Invar-alloy frame and the aluminum sheet can generate a temperature-dependent anisotropic strain, reaching $\varepsilon = \varepsilon_V - \varepsilon_H \approx 0.6\%$ at base temperature [26], which is large enough to detwin FeSe with orthorhombic lattice distortion $\delta = [(a_o - b_o)]/[(a_o + b_o)] \approx 0.27\%$ (corresponding to $\varepsilon \approx 0.54$) at $T \ll T_s$ [43]. Neutron diffraction measurements on 26 pieces of FeSe crystals (25 mg) glued on one uniaxial-strain device reveals a detwinning ratio $\eta = \frac{P_1 - P_2}{P_1 + P_2} \approx 71\%$ (for details see the Supplementary Information) [26], where P_1 and P_2 represent the relative population of the two kinds of twin domains. For the samples used for INS experiments, we use the low-energy spin excitations at $E = 4 \pm 1$ meV and 10 ± 2 meV to estimate the detwinning ratio and find the samples are highly detwinned with $\eta \approx 58\%$ ($P_1/P_2 \approx 3.75$) (for details see the Supplementary Information) [26].

Spin excitations of detwinned FeSe at low temperature

Figure 1(c) shows one-dimensional (1D) constant-energy cuts with $E = 55 \pm 10$ meV along the $[1, K]$ (red diamonds) and $[H, 1]$ (blue squares) directions measured on Sample #1. The same cuts on Sample #2 are presented in Fig. 1(d). In both panels, the integrated intensity of the stripe excitations around $(1, 0)$ is ~ 3 times of that around $(0, 1)$, indicating a large spin-excitation anisotropy. For comparison, the Néel excitations at $(\pm 1, \pm 1)$ are identical in lineshape and intensity. This confirms the C_2 symmetry of the stripe excitations reported in previous INS and RIXS studies [24, 25] and demonstrates that the Néel spin excitations are C_4 symmetric in the nematic state.

Figure 2 reveals the energy and wave-vector dependence of the spin excitations of detwinned FeSe measured at base temperature. Figures 2(a)-2(d) show the spin excitations for $E_i = 147.5$ meV projected onto (\mathbf{Q}, E) planes with \mathbf{Q} along

the $[1, K]$, $[H, 0]$, $[H, 1]$, and $[0, K]$ directions, respectively. The scattering of an empty strain device (with CYTOP) measured under the same conditions has been subtracted from the data, leading to the clear spin excitation dispersions below $E = 100$ meV in Figs. 2(a)-2(d) (see the Supplementary Information) [26]. Despite the absence of a stripe order, spin excitations arising from the stripe-order wavevector $(1, 0)$ are much stronger than the excitations emanating from the $(0, 1)$ and the C_4 -symmetric Néel spin excitations at the $(\pm 1, \pm 1)$ positions (Figs. 2(a)-(d)). The energy-dispersion branches along the $[1, K]$ direction of the stripe excitations are very sharp (Fig. 2(a)), while the stripe excitations in Figs. 2(b) and 2(d) are along the longitudinal $[H, 0]$ and $[0, K]$ direction appear non-dispersive and damped. Similar anisotropic damping of the stripe excitations between the $[1, K]$ and $[H, 0]$ directions was observed in CaFe_2As_2 [33], BaFe_2As_2 [13], and NaFeAs [29]. While a clear dispersion along $[H, 0]$ can persist to $E \approx 150$ meV in CaFe_2As_2 and $E \approx 100$ meV for BaFe_2As_2 , it was damped so quickly that no dispersive feature can be resolved in NaFeAs . The highly anisotropic damping of the stripe excitations in FeSe is much akin to that in NaFeAs . As we will discuss later, the much stronger anisotropic damping in FeSe and NaFeAs could be attributed to the large anion height (h_{FeX}) in these two materials that control the electron-correlation magnitude in the d_{xy} orbital (Fig. 1(e)) [27, 34].

Figures 2(e)-2(n) are constant-energy intensity maps of the spin excitations in the $[H, K]$ plane, confirming again the C_2 and C_4 symmetry of the stripe and the Néel excitations, respectively. The stripe spin excitations at $(1, 0)$ are isotropic in momentum space at the low-energy range $E \lesssim 15$ meV (Figs. 2(e)-(f)), but exhibit anisotropic dispersion and damping at $E \gtrsim 20$ meV. They propagate well along the $[1, K]$

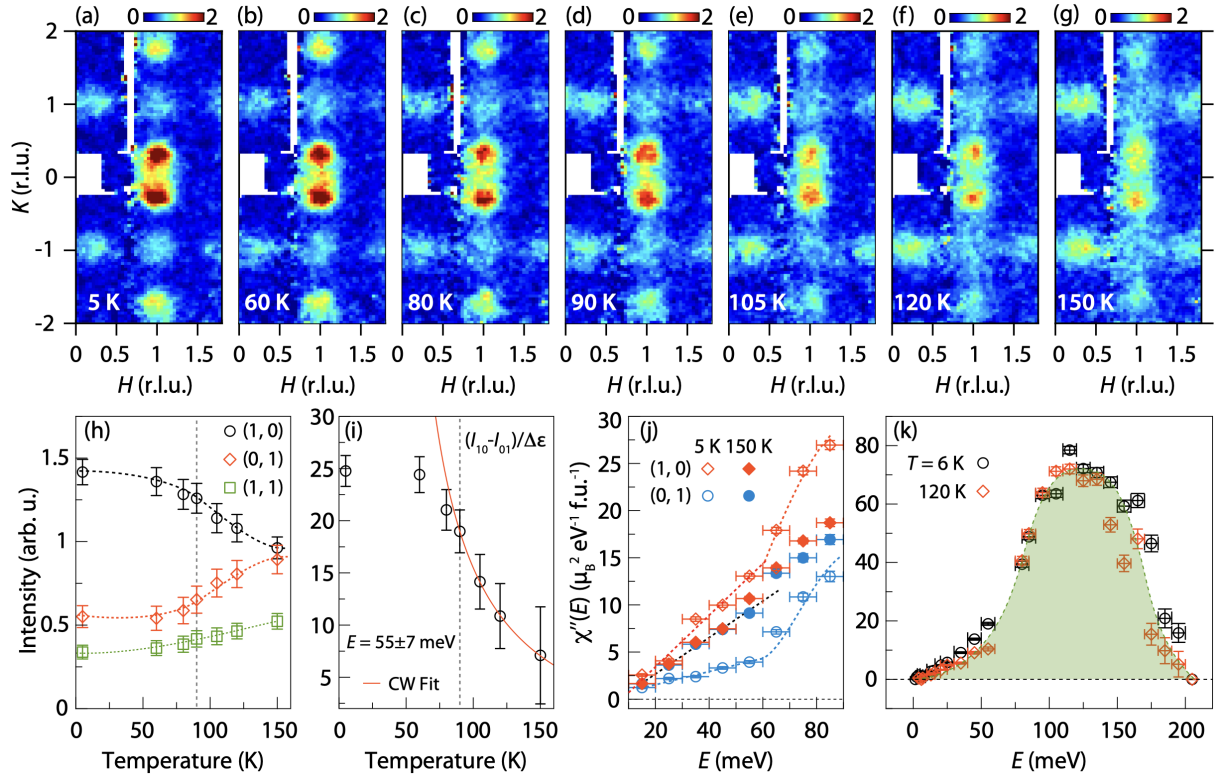


FIG. 3: **Temperature dependence of the magnetic excitations in detwinned FeSe.** Constant energy slices of the magnetic excitations for detwinned FeSe single crystals with $E = 55 \pm 7$ meV at $T = 5$ K, 60 K, 80 K, 90 K, 105 K, 120 K and 150 K. The background scattering collected from an empty strain device with CYTOP has been subtracted from the data (a)-(g). (h) Temperature dependence of the integrated intensities of the magnetic excitations at $\mathbf{Q} = (1, 0)$ (denoted by I_{10}), $(0, 1)$ (denoted by I_{01}) and $(1, 1)$ with $E = 55 \pm 7$ meV. Dashed curves are guides to the eyes. (i) Strain normalized nematic spin correlation $\Delta\psi(E, T)/\Delta\varepsilon = (I_{10} - I_{01})/\Delta\varepsilon$ with $E = 55 \pm 7$ meV. The red curve is a Curie-Weiss fitting of the data at $T = 90 - 150$ K with $\Delta\psi(E)/\Delta\varepsilon = \lambda/[a_0(T - T^*) + b_0] + \chi_0$. The vertical dashed lines in (h) and (i) mark the unstrained $T_s = 90$ K. (j) Comparison of local susceptibility $\chi''(E)$ (momentum averaged $\chi''(\mathbf{Q}, E)$) for detwinned FeSe single crystals at $\mathbf{Q} = (1, 0)$ and $(0, 1)$, measured at $T = 5$ K (open symbols) and 150 K (filled symbols). The data is corrected with the magnetic form factor and Bose factor. The dashed curves are guides to the eyes. (k) Energy dependence of local dynamic susceptibility $\chi''(E)$ for detwinned FeSe single crystals at $T = 6$ K (black open circles) and 120 K (red open diamond). The horizontal and vertical error bars indicate the energy integration range for calculating $\chi''(E)$ and the statistical errors of one standard deviation. The data in (a)-(j) were collected on SEQUOIA with $E_i = 147.5$ meV. The data in (k) was collected on 4SEASONS with $E_i = 21, 36, 80$ and 295 meV).

direction but damp quickly along the $[H, 0]$ direction, consistent with the energy-momentum slices in Figs. 2(a)-2(d). The Néel excitations are visible at $E \gtrsim 40$ meV (Figs. 2(h)-2(j)) and merge with the stripe excitations at $E \gtrsim 90$ meV. The anisotropy between the stripe excitations at $(1, q_1)$ and $(q_2, 1)$ persists to $E = 120 \pm 10$ meV and vanishes at higher energies, leaving four-fold symmetric broad scattering at around $(\pm 1, \pm 1)$ in Figs. 2(m) ($E = 140 \pm 10$ meV) and 2(n) ($E = 160 \pm 10$ meV).

The intensity difference between the spin excitations at $\mathbf{Q}_1 = (1, q_1)$ and $\mathbf{Q}_2 = (q_2, 1)$ in the nematic state, termed nematic spin correlations, is defined as $\psi(E) = [S(\mathbf{Q}_1, E) - S(\mathbf{Q}_2, E)]/[S(\mathbf{Q}_1, E) + S(\mathbf{Q}_2, E)]$ (or defined via the imaginary part of the dynamic susceptibility $\chi''(\mathbf{Q}, E)$ in the same way) [13]. It was indirectly probed by RIXS in the limited region of the first BZ at the Γ point [25]. Here we conclusively determine the energy scale of the nematic spin correlations as $E \approx 120 \pm 10$ meV, roughly consistent with that ($E \approx 200$

meV) determined in the RIXS study of detwinned FeSe [25].

Temperature dependence of the spin excitations

The nematic spin correlation $\psi(E, T)$ is a manifestation of the electronic nematicity in the spin-spin correlation function and represents the nematic order parameter in the spin channel [3]. Its temperature dependence across the nematic transition will provide more evidence concerning the origin of the nematic order. Figures 3(a)-3(g) show the temperature dependence of the stripe and the Néel spin excitations in the energy range $E = 55 \pm 7$ meV, measured at $T = 5, 60, 80, 90, 105, 120$, and 150 K. The integrated intensities as a function of temperature are shown in Fig. 3(h). The Néel excitations with smaller spectral weight increase slightly from 5 K to 150 K. On warming from $T = 5$ K to 150 K, the stripe excitations at $(1, 0)$ decrease, whereas the excitations at $(0, 1)$ increase gradually, leading to a diminishing $\psi(E)$. No sudden change occurs for the stripe and the Néel excitations at the unstrained $T_s = 90$

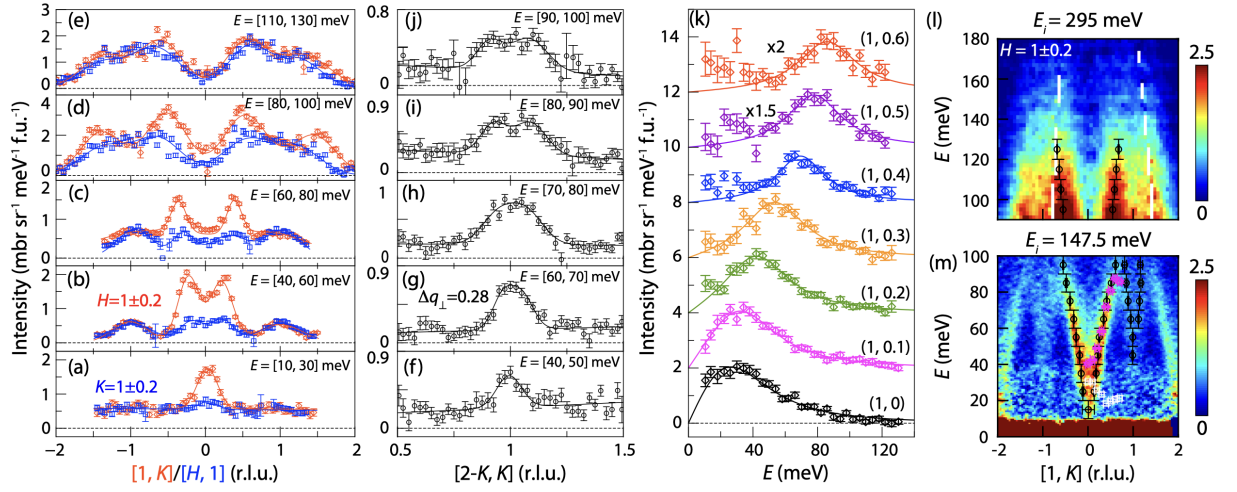


FIG. 4: **One-dimensional cuts and energy dispersion of the magnetic excitations in detwinned FeSe.** (a)-(j) Constant-energy cuts along the $[1, K]$, $[H, 1]$, and $[2 - K, K]$ directions across the $\mathbf{Q} = (1, 0)$ and $(0, 1)$ ((a)-(e)) and $\mathbf{Q} = (1, 1)$ ((f)-(j)) for detwinned FeSe single crystals at base temperature. The integral intervals perpendicular to the cut directions are $H = 1 \pm 0.2$, $K = 1 \pm 0.2$, and $\Delta q_{\perp} = 0.28$ r.l.u., respectively. (k) Constant- \mathbf{Q} cuts ($E_i = 147.5$ meV, $T = 5$ K) at $\mathbf{Q} = (1, q \pm 0.05)$ ($q = 0, 0.1, \dots, 0.6$). The data are fitted by a general damped harmonic oscillator model (solid curves). (l)-(m) Magnetic excitation dispersions along $[1, K]$ directions projected onto energy and momentum planes measured on (l) Sample #2 with $E_i = 295$ meV, $T = 6$ K and (m) Sample #1 with $E_i = 147.5$ meV, $T = 5$ K. The black circle symbols represent the magnetic excitation dispersions at $\mathbf{Q} = (1, 0)$ and $(1, 1)$, which are the Gaussian function fitting results of one-dimensional constant-energy cuts.

K , possibly because the structural transition is smeared out under the uniaxial strain [35]. Note that the uniaxial strain decreases gradually with increasing temperature and could be reduced by $\sim 40\%$ at $T = 150$ K.

The persistent $\psi(E)$ at $T > T_s$ induced by moderate uniaxial strain ($\varepsilon \sim 0.3\%$) in the nematic fluctuating regime has been indirectly probed in a prior RIXS study of $\text{FeSe}_{1-x}\text{S}_x$ [36]. Here, to obtain a quantitative understanding of $\psi(E, T \gtrsim T_s)$, we characterized the temperature-dependent uniaxial strain on a FeSe single crystal glued on a similar device using an optical method (see the Supplementary Information) [26] and got strain-normalized $\Delta\psi(E)/\Delta\varepsilon = (I_{10} - I_{01})/\Delta\varepsilon$ for $E = 55 \pm 7$ meV (Fig. 3(i)), which represents the nematic susceptibility in the spin (fluctuation) channel. The $\Delta\psi(E)/\Delta\varepsilon$ at $T \gtrsim T_s$ can be well described by a Curie-Weiss behavior $\Delta\psi(E)/\Delta\varepsilon = \lambda/[a_0(T - T^*) + b_0] + \chi_0$ (red curve in Fig. 3(i)), which generates a bare nematic transition temperature $T^* \approx 34$ K. This T^* value is consistent with the Weiss temperature obtained by fitting the static nematic susceptibility derived from the elastoresistance measurements of FeSe [37]. This further demonstrates that the electronic nematicity is driven by spin fluctuations [25, 36].

Figure 3(j) shows the temperature-dependent $\chi''(E)$ for the energy range $E \lesssim 90$ meV measured on sample #1 at SE-QUOIA. The nematic stripe spin correlation $([\chi''(\mathbf{Q}_1, E) - \chi''(\mathbf{Q}_2, E)]/[\chi''(\mathbf{Q}_1, E) + \chi''(\mathbf{Q}_2, E)])$ retains its magnitude at energies up to 90 meV at $T = 5$ K and almost vanishes at $T = 150$ K well above the unstrained T_s under a moderate uniaxial strain (Fig. S6 in the Supplementary Information) [26].

Analysis of the spin-excitations in FeSe

A surprising discovery in the spin excitations is the linear-in-energy spectral weight (local dynamic susceptibility $\chi''(E)$) at the energy range $E \lesssim 60$ meV measured at $T \ll T_s$ and the temperature ($T = 150$ K) well above T_s (Figs. 3(j)-(k)). Some of us considered an $S = 1$ generalized bilinear-biquadratic model on a square lattice and proposed that an $(\pi, 0)$ AFQ state could describe the magnetism in bulk FeSe [22, 32]. The linear energy dependence of the low-energy $\chi''(E)$ was an essential prediction/feature associated with the AFQ order, providing a clue to understanding the magnetic ground state, as we will discuss later.

Figure 3(k) shows the twin-domain averaged $\chi''(E)$ for the full energy range measured on Sample #2 at 4SEASONS. It is consistent in lineshape with but shows ($\sim 30\%$) higher peak intensity than that measured on a twinned sample [20]. The integral of the total spectral weight of $\chi''(E)$ generates the fluctuating moments $\langle m^2 \rangle = 7.45 \pm 0.25 \mu_B^2$ at $T = 6$ K, and $6.23 \pm 0.34 \mu_B^2$ at $T = 120$ K. Following the magnetic moment sum rule $\langle m^2 \rangle = g^2 \mu_B^2 S(S + 1)$ and with $g = 2$ [2], we get $S \approx 0.95 \pm 0.06$ for $T = 6$ K and $S \approx 0.84 \pm 0.08$ for $T = 120$ K, corroborating the $S = 1$ localized spin scenario for FeSe [20].

To obtain a quantitative understanding of the spin excitations, we plot in Figs. 4(a)-4(e) the constant-energy momentum cuts across $(1, 0)$, $(0, 1)$, and $(1, 1)$ along the $[1, K]$ and $[H, 1]$ directions, with $E = 20 \pm 10, 50 \pm 10, 70 \pm 10, 90 \pm 10$, and 120 ± 10 meV, and in Figs. 4(f)-4(j) the momentum cuts along a diagonal $[2 - K, K]$ direction with $E = 45 \pm 5, 65 \pm 5$,

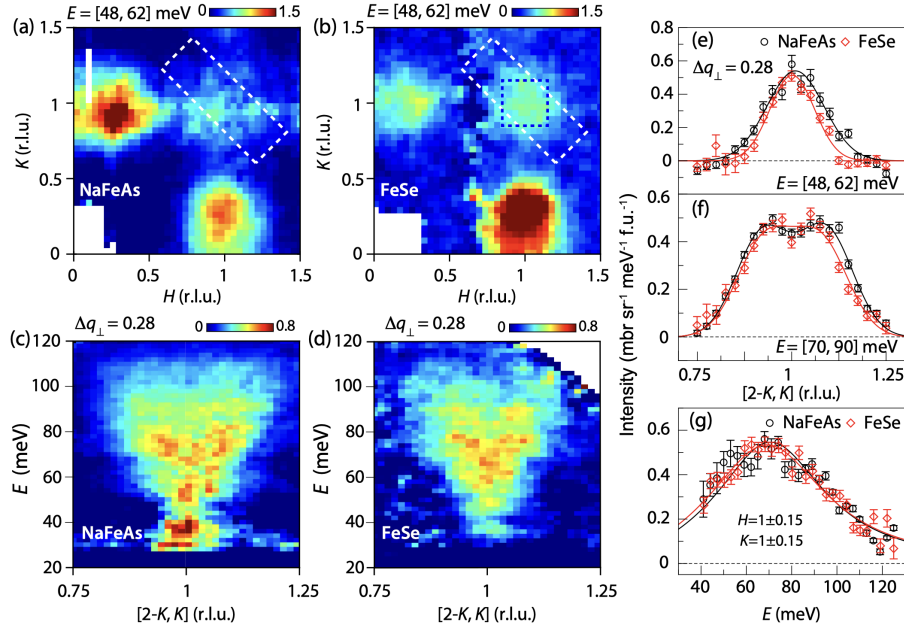


FIG. 5: **Comparison of the Néel excitations in NaFeAs and FeSe.** (a), (b) Constant-energy slices of the spin excitations in twinned NaFeAs ($E = 55 \pm 7$ meV) (a), collected with $E_i = 150$ meV and detwinned FeSe ($E = 55 \pm 7$ meV) (b), collected with $E_i = 147.5$ meV. (c), (d) spin-excitation dispersion along the transverse direction $[2 - K, K]$ (dashed rectangles in (a)-(b)) across the $\mathbf{Q} = (1, 1)$ in twinned NaFeAs (c) and detwinned FeSe (d). (e), (f) Constant energy cuts along the $[2 - K, K]$ direction for NaFeAs (black open circles) and FeSe (red open diamonds) with $E = 55 \pm 7$ meV (e), and $E = 80 \pm 10$ meV (f). The integral interval perpendicular to $[2 - K, K]$ is $\Delta q_{\perp} = 0.28$. (g) Energy cuts at $\mathbf{Q} = (1 \pm 0.15, 1 \pm 0.15)$ (marked by the blue dashed square in Fig 5(b)) for NaFeAs and FeSe.

75 ± 5 , 85 ± 5 , and 95 ± 5 meV. The fit of the constant-energy momentum cuts with multi-Gaussian functions generates the energy dispersions of the stripe and the Néel spin excitations, which are plotted onto the E -vs- $[1, K]$ slices in Figs. 4(l)-(m), where the stripe and the Néel excitations are resolved for energies up to $E \approx 125$ meV. We note that the Néel excitations touch the stripe excitation branch around $E \approx 90$ meV while the latter persist to $E \approx 130$ meV and dominate the spectral weight, indicating that they are indeed separate excitations arising from the competing stripe and Néel magnetic interactions [20].

In Fig. 4(k), we use a general damped harmonic oscillator function to describe $\chi''(\mathbf{Q}, E) = A \frac{2\gamma E E_0}{(E^2 - E_0^2)^2 + (\gamma E)^2}$ and fit the energy cuts at $\mathbf{Q} = (1, q \pm 0.05)$ ($q = 0, 0.1, \dots, 0.6$) with $S(\mathbf{Q}, E) = \chi''(\mathbf{Q}, E) f^2(\mathbf{Q})$ (solid curves in Fig. 4(k)), where $E_0(q)$ is the undamped energy, $\gamma(q)/2$ is the damping rate, and $f(\mathbf{Q})$ the magnetic form factor of Fe^{2+} . The resulting damping rates $\gamma/2$ (white open squares in Fig. 4(m)) are much smaller than the undamped energies (magenta open diamonds in Fig. 4(l)), indicating the stripe excitations are only slightly damped for $q \leq 0.7$. This is unprecedented strong evidence supporting the localized spin picture in FeSe. Thus, our results demonstrate that the $S = 1$ localized spin picture is a correct starting point for describing the magnetism in FeSe, and it is likely that the magnetic state in FeSe is intimately connected with the AFQ regime.

The Néel spin excitations

In iron-based superconductors, the Néel spin excitation at $(\pm 1, \pm 1)$ is not unique to FeSe, but had already been observed in NaFeAs hosting a static stripe order ($T_N \approx 45 < T_s = 58$ K) with the ordered magnetic moment $M = 0.17 \pm 0.034 \mu_B/\text{Fe}$ and the total fluctuating moment $\langle m^2 \rangle = 3.6 \mu_B^2$ ($S \approx 0.57$) [29, 38, 39]. Figures 5(a)-5(g) show the comparison of the Néel spin excitations in NaFeAs and FeSe, measured with $E_i = 150$ meV on the ARCS spectrometer, and $E_i = 147.5$ meV on the SEQUOIA spectrometer, respectively. Figures 5(a) and 5(b) show magnetic excitations projected onto the $[H, K]$ plane with $E = 55 \pm 7$ meV, in which similar Néel excitations at $(1, 1)$ are visible in both NaFeAs (Fig. 5(a)) and FeSe (Fig. 5(b)). The Néel excitations projected onto the E -vs- $[2 - K, K]$ plane (Figs. 5(c) and 5(d)) also exhibit similar "V"-shaped dispersion. Furthermore, the constant-energy cuts across $(1, 1)$ along the $[2 - K, K]$ direction at $E = 55 \pm 7$ meV (Fig. 5(e)) and $E = 80 \pm 10$ meV (Fig. 5(f)), and the energy cut at the $\mathbf{Q} = (1, 1)$ show that the Néel excitations in NaFeAs and FeSe are almost identical.

In addition, the stripe excitations of FeSe and NaFeAs exhibit similar anisotropic damping along the $[1, K]$ (transverse) and the $[H, 0]$ (longitudinal) directions, and similar much lower band top along the $[1, K]$ direction ($E \sim 100$ meV) than BaFe_2As_2 ($E \sim 200$ meV) [29, 39]. Figures 1(e) and 1(f) plot the systematic changes of the ordered moment ($\langle m \rangle$), the fluctuating moment ($\langle m^2 \rangle$), and the electron correlation (m^*/m_{band}) of these three compounds as a function of the anion height Fe-X ($X = \text{As, Se}$) (h_{FeX}), suggesting that the larger

h_{FeX} in NaFeAs and FeSe (compared to BaFe₂As₂) enhance the electron correlations in the d_{xy} orbital [27, 29]. This has been used to explain small bandwidth along $[1, K]$ in FeSe and NaFeAs [27, 29, 39]. As the Néel excitations are absent in BaFe₂As₂ and related materials, it is natural to speculate that the Néel excitations are also associated with the d_{xy} orbital with enhanced electron correlations.

In electron-doped NaFe_{1-x}Co_xAs, while the low-energy stripe excitations associated with Fermi surface nesting evolve with the topology changes of the Fermi surfaces driven by electron doping, the relatively high energy ($E \gtrsim 50$ meV) stripe excitations, as well as the Néel excitations, remain essentially unchanged across the whole superconducting regime ($x = 0 - 0.11$) [39]. These results suggest that superconductivity is coupled to the low-energy stripe excitations but not the Néel excitations. We note that the iron pnictogen height in (h_{FeAs}) decreased by less than 1% from $x = 0$ to 0.11 [40], consistent with the invariance of the Néel excitations. In addition, several studies suggest that the stripe order could be “restored” in FeSe under $P \gtrsim 1$ GPa hydrostatic pressure that reduces the anion height slightly [23, 41–43]. Therefore, the h_{FeX} could drive the ground state of FeSe across a phase boundary associated with the stripe order, and the pressured FeSe ($P \gtrsim 1$ GPa) with stripe order fills the gap between FeSe and NaFeAs in Figs. 1(f) and 1(g).

The spin-interaction phase diagram

To achieve a better understanding of the magnetic ground state in FeSe, we use a minimal $S = 1$ J_1 - K - J_2 model to fit the energy dispersions of the stripe spin excitations in FeSe, NaFeAs, and BaFe₂As₂ in Fig. 1(e). To improve the accuracy of the fittings, we include the dispersion near the Γ point measured with RIXS (data points between (0, 0) and (0, 0.5)) [25, 28]. The fitting of the dispersion for BaFe₂As₂ is a reference to show the validity of the fitting strategy. Previously, the fitting of the $S(\mathbf{Q}, E)$ in twinned BaFe₂As₂ with the J_{1a} - J_{1b} - J_2 ($-J_c$) model generates $J_{1a} = 59.2$, $J_{1b} = -9.2$ and $J_2 = 13.6$ meV, corresponding to $J_1 = 25$ meV, $K = 17.1$ meV ($J_{1a} = J_1 + 2K$, $J_{1b} = J_1 - 2K$), $J_2/J_1 \approx 0.54$ and $K/J_1 \approx 0.68$ in the J - K model. In comparison, the fitting of the energy dispersion of BaFe₂As₂ in Fig. 1(e) gives $J_1 = 23.5$ meV, $K = 16.1$ meV and $J_2 = 15$ meV ($J_2/J_1 \approx 0.64$ and $K/J_1 \approx 0.69$), agrees well with the fitting of the $S(\mathbf{Q}, E)$ in twinned BaFe₂As₂.

For FeSe (NaFeAs), the fitting of the energy dispersion provides $J_1 = 29.9$ (28.8) meV, $K = 11.9$ (11.2) meV, and $J_2 = 11.0$ (13.4) meV, leading to $J_2/J_1 \approx 0.37$ (0.47) and $K/J_1 \approx 0.40$ (0.39). The J_2/J_1 of FeSe is close to that ($J_2/J_1 = 0.413$) reported in ref. [44]. FeSe shows slightly larger J_1 and K and smaller bandwidth than NaFeAs, further indicating the electron correlation in FeSe is slightly stronger than the other compounds (Fig. 1(f)).

We plot in Fig. 1(h) the trend in the magnetic interactions J_2/J_1 and K/J_1 of FeSe, NaFeAs, and BaFe₂As₂. It is well known that BaFe₂As₂ is deep in the stripe-ordering region. NaFeAs hosting a weak stripe order accompanied by the Néel

excitations should already be close to the cross-over between the stripe and the Néel regime. For FeSe, as the AFQ model can describe the linear-in-energy $\chi''(E)$ for $E \lesssim 60$ meV and C_2 symmetry of the stripe excitations, it should be near the AFQ ordering regime. Meanwhile, FeSe is close to NaFeAs in the phase diagram and exhibits also the Néel excitations. Thus, it should also be close to both the stripe and the Néel ordering regimes. All these key features can be qualitatively described in a zero-temperature phase diagram containing the stripe order, Néel order, and AFQ order generated by a $S = 1$ bilinear-biquadratic J_1 - J_2 - K model, as shown in Fig. 1(h) [45]. We find that: (1) both K/J_1 and J_2/J_1 are essential in tuning the magnetic ground states; (2) J_2/J_1 plays a key role in driving the ground state from the stripe ordering region to the AFQ regime; and (3) FeSe is positioned close to a crossover regime where the AFQ, Néel, and stripe orders intersect [45].

In summary, our INS results on the uniaxial-strain detwinned FeSe clarify the symmetry of the stripe and the Néel spin excitations, characterize the nematic spin correlations, determine the magnetic interactions, and establish the evolution of the magnetic ground state in iron-based superconductors. The uniaxial-strain device suitable for INS developed in this work could also detwin or even apply uniaxial-strain on similar magnetic materials with layered structures.

Methods

Sample preparation The FeSe single crystals used in the present study were grown using the chemical vapor transport method. The direction of the self-cleaving edges of the FeSe crystals is tetragonal $[1, 0, 0]$, as determined with a Laue camera. We co-aligned and glued ~ 1500 pieces ($m_1 \approx 1.61$ grams) of thin FeSe crystals onto ten (20×22 mm²) areas (the front and back sides of 5 aluminum sheets) along the tetragonal $[1, 1, 0]$ direction using the hydrogen-free CYTOP, which were installed onto the invar alloy frames to form the Sample #1 used in the neutron scattering experiments on SE-QUOIA and MAPS time-of-flight spectrometers. We also prepared a Sample #2 following the same way, which contained ~ 1000 pieces ($m_2 \approx 1.24$ grams) of thin FeSe crystals and was used in the neutron scattering experiment on the Fermi chopper spectrometer 4SEASONS.

Neutron scattering experiments The INS experiments were performed on the SEQUOIA [46], 4SEASONS [47], and MAPS [48] time-of-flight spectrometers at the Spallation Neutron Source at the Oak Ridge National Laboratory (ORNL), Materials and Life Science Experimental Facility (MLF) at the Japan Proton Accelerator Research Complex (J-PARC), and the ISIS spallation neutron source, Rutherford Appleton Laboratory (RAL), respectively. We defined the wave vector \mathbf{Q} in reciprocal space as $\mathbf{Q} = H\mathbf{a}^* + K\mathbf{b}^* + L\mathbf{c}^*$, where H, K, L are Miller indices and $\mathbf{a}^* = \hat{\mathbf{a}} 2\pi/a_o$, $\mathbf{b}^* = \hat{\mathbf{b}} 2\pi/b_o$, and $\mathbf{c}^* = \hat{\mathbf{c}} 2\pi/c$ are reciprocal lattice unit (r.l.u.) vectors with $a_o \approx 5.33$ Å, $b_o \approx 5.31$ Å and $c \approx 5.49$ Å.

Author contributions

X.L. conceived this project and designed the uniaxial-strain device. R.L. grew and coaligned the crystals. R.L., M.B.S., S.G. M.N., K.K., A.K., H.C.W., and X.L. performed the inelastic neutron scattering experiments. R.L., P.C., and X.L. performed the neutron diffraction measurements. R.L. and X.L. analysed the data. R.Y. and Q.S. carried out theoretical and computational analyses. X.L. wrote the manuscript with inputs from R.L, P.D., R.Y., and Q.S. All authors made comments.

Acknowledgement

The work at Beijing Normal University is supported by National Key Projects for Research and Development of China with Grant No. 2021YFA1400400 and the National Natural Science Foundation of China (grants nos. 12174029, and 11922402) (X.L.). The work at Renmin University of China is supported by the National Science Foundation of China Grant No. 12174441. P.D. is supported by the U.S. DOE, BES under grant no. DESC0012311. Q.S. is primarily supported by the U.S. DOE, BES under Award No. DE-SC0018197, and by the Robert A. Welch Foundation Grant No. C-1411. This research used resources at Spallation Neutron Source, a U.S. DOE Office of Science User Facility operated by ORNL. We acknowledge the neutron beam time from J-PARC with Proposal No. 2019A0002. We gratefully acknowledge the Science and Technology Facilities Council (STFC) for access to neutron beam time at ISIS [49].

* Electronic address: pdai@rice.edu

† Electronic address: luxy@bnu.edu.cn

- [1] Scalapino, D. J. A common thread: The pairing interaction for unconventional superconductors *Rev. Mod. Phys.* **84**, 1383-1417 (2012).
- [2] Dai, P. Antiferromagnetic order and spin dynamics in iron-based superconductors. *Rev. Mod. Phys.* **87**, 855-896 (2015).
- [3] Fernandes, R. M., Chubukov, A. V. & Schmalian, J. What drives nematic order in iron-based superconductors? *Nat. Phys.* **10**, 97-104 (2014).
- [4] Q. Si, R. Yu, & E. Abrahams, High Temperature Superconductivity in Iron Pnictides and Chalcogenides. *Nat. Rev. Mater.* **1**, 16017 (2016).
- [5] Q. Si & N. E. Hussey, Iron-based superconductors: Teenage, complex, challenging. *Phys. Today* **76** (5), 34-40 (2023).
- [6] Fernandes, R. M. et al. Iron pnictides and chalcogenides: a new paradigm for superconductivity. *Nature* **601** 35-44 (2022).
- [7] Böhmer, A. E., Chu, J.-H., Lederer, S., & Yi, M. Nematicity and nematic fluctuations in iron-based superconductors. *Nat. Phys.* **18**, 1412-1419 (2022).
- [8] Chu, J.-H. et al. In-plane resistivity anisotropy in an underdoped iron arsenide superconductor. *Science* **329**, 824-826 (2010).
- [9] Yi, M. et al. Symmetry-breaking orbital anisotropy observed for detwinned $\text{Ba}(\text{Fe}_{1-x}\text{Co}_x)_2\text{As}_2$ above the spin density wave transition. *Proc. Natl Acad. Sci. USA* **108**, 6878-6883 (2011).
- [10] Chu, J.-H., Kuo, H.-H., Analytis, J. G., & Fisher, I. R. Divergent Nematic Susceptibility in an Iron Arsenide Superconductor, *Science* **337**, 710 (2012).
- [11] Kuo, H.-H., Chu, J.-H., Palmstrom, J. C., Kivelson, S. A., & Fisher, I. R. Ubiquitous signatures of nematic quantum criticality in optimally doped Fe-based superconductors. *Science* **352**, 958-962 (2016).
- [12] Lu, X. et al. Nematic spin correlations in the tetragonal state of uniaxial-strained $\text{BaFe}_{2-x}\text{Ni}_x\text{As}_2$, *Science* **345**, 657 (2014).
- [13] Lu, X. et al. Spin waves in detwinned BaFe_2As_2 . *Phys. Rev. Lett.* **121**, 067002 (2018).
- [14] Hsu, F. C. et al. Superconductivity in the PbO-type structure α -FeSe. *Proc. Natl Acad. Sci. USA* **105**, 14262 (2008).
- [15] McQueen, T. M. et al. Tetragonal-to-orthorhombic structural phase transition at 90K in the superconductor $\text{Fe}_{1.01}\text{Se}$. *Phys. Rev. Lett.* **103**, 057002 (2009).
- [16] Wang, Q. et al. Strong interplay between stripe spin fluctuations, nematicity and superconductivity in FeSe. *Nat. Mater.* **15**, 159 (2016).
- [17] Tanatar, M. A. et al. Origin of resistivity anisotropy in the nematic phase of FeSe. *Phys. Rev. Lett.* **117**, 127001 (2016).
- [18] Coldea, A. & Watson M. D. The key ingredients of the electronic structure of FeSe. *Annu. Rev. Condens. Matter Phys.* **9**, 125-146 (2018).
- [19] Harriger, L. W. et al. Nematic spin fluid in the tetragonal phase of BaFe_2As_2 . *Phys. Rev. B* **84**, 054544 (2011).
- [20] Wang, Q. et al. Magnetic ground state of FeSe. *Nat. Commun.* **7**, 12182 (2016).
- [21] Wang, F., Kivelson, S. & Lee, D.-H. Nematicity and quantum paramagnetism in FeSe. *Nat. Phys.* **11**, 959-963 (2015).
- [22] Yu, R. & Si, Q. Antiferroquadrupolar and Ising-nematic orders of a frustrated bilinear-biquadratic Heisenberg model and implications for the magnetism of FeSe. *Phys. Rev. Lett.* **115**, 116401 (2015).
- [23] Glasbrenner, J. K. et al. Effect of magnetic frustration on nematicity and superconductivity in iron chalcogenides. *Nat. Phys.* **11**, 953 (2015).
- [24] Chen, T. et al. Anisotropic spin fluctuations in detwinned FeSe. *Nat. Mater.* **18**, 709-716 (2019).
- [25] Lu, X. et al. Spin-excitation anisotropy in the nematic state of detwinned FeSe. *Nat. Phys.* **18**, 806-812 (2022).
- [26] See the supplemental materials for details.
- [27] Yin, Z. P., Haule, K., and Kotliar G. Kinetic frustration and the nature of the magnetic and paramagnetic states in iron pnictides and iron chalcogenides. *Nat. Mater.* **10**, 932-935 (2011).
- [28] Pellicciari, J. et al. Intralayer doping effects on the high-energy magnetic correlations in NaFeAs . *Phys. Rev. B* **93**, 134515 (2016).
- [29] Zhang, C. et al. Effect of Pnictogen Height on Spin Waves in Iron Pnictides. *Phys. Rev. Lett.* **112**, 217202 (2014).
- [30] Wysocki, A. L., Belashchenko, K. D., & Antropov, V. P. Consistent model of magnetism in ferropnictides. *Nat. Phys.* **7**, 485-489 (2011).
- [31] Yu, R., Wang, Z., Goswami, P., Nevidomskyy, A. H., Si, Q., & Abrahams, E. Spin dynamics of a J_1 - J_2 - K model for the paramagnetic phase of iron pnictides. *Phys. Rev. B* **86**, 085148 (2012).
- [32] Lai, H.-H., Hu, W.-J., Nica, E.-M., Yu, R., & Si, Q. Antiferroquadrupolar Order and Rotational Symmetry Breaking in a Generalized Bilinear-Biquadratic Model on a Square Lattice. *Phys. Rev. Lett.* **118**, 176401 (2017).
- [33] Zhao, J. et al. Spin waves and magnetic exchange interactions in CaFe_2As_2 .
- [34] Yu, R. & Si, Q. Orbital-Selective Mott Phase in Multiorbital Models for Alkaline Iron Selenides $\text{K}_{1-x}\text{Fe}_{2-y}\text{Se}_2$. *Phys. Rev. Lett.* **110**, 146402 (2013).
- [35] Lu, X. et al. Impact of uniaxial pressure on structural and magnetic phase transitions in electron-doped iron pnictides. *Phys.*

- Rev. B* **93**, 134519 (2016).
- [36] Liu, R. et al. Nematic spin correlations pervading the phase diagram of $\text{FeSe}_{1-x}\text{S}_x$. arXiv:2307.08181.
- [37] Hosoi, S. et al. Nematic quantum critical point without magnetism in $\text{FeSe}_{1-x}\text{S}_x$ superconductors. *Proc. Natl Acad. Sci. USA* **113**, 8139-8143 (2016).
- [38] Tan, G. et al. Electron doping evolution of structural and antiferromagnetic phase transitions in $\text{NaFe}_{1-x}\text{Co}_x\text{As}$ iron pnictides. *Phys. Rev. B* **94**, 014509 (2016).
- [39] Carr, S. V. Electron doping evolution of the magnetic excitations in $\text{NaFe}_{1-x}\text{Co}_x\text{As}$. *Phys. Rev. B* **93**, 214506 (2016).
- [40] Parker, D. et al. Control of the Competition between a Magnetic Phase and a Superconducting Phase in Cobalt-Doped and Nickel-Doped NaFeAs Using Electron Count. *Phys. Rev. Lett.* **104**, 057007 (2010).
- [41] Wang, P. S. et al. Pressure induced stripe-order antiferromagnetism and first-order phase transition in FeSe . *Phys. Rev. Lett.* **117**, 237001 (2016).
- [42] Sun, J. P. et al. Dome-shaped magnetic order competing with high-temperature superconductivity at high pressures in FeSe . *Nat. Commun.* **7**, 12146 (2016).
- [43] Kothapalli, K. et al. Strong cooperative coupling of pressure-induced magnetic order and nematicity in FeSe . *Nat. Commun.* **7**, 12728 (2016).
- [44] Gu, Y. et al. Frustrated magnetic interactions in FeSe . *Phys. Rev. B* **106**, L060504 (2022).
- [45] Hu, W.-J., Lai, H.-H., Gong, S.-S., Yu, R., Dagotto, E., & Si, Q. Quantum transitions of nematic phases in a spin-1 bilinear-biquadratic model and their implications for FeSe . *Phys. Rev. Res.* **2**, 023359 (2020).
- [46] Granroth, G.E. et al. SEQUOIA: a newly operating chopper spectrometer at the SNS. *J. Phys.: Conf. Ser.* **251**, 12058 (2010).
- [47] Kajimoto, R. et al. The Fermi Chopper Spectrometer 4SEASONS at J-PARC. *J. Phys. Soc. Jpn.* **80**, SB025 (2011).
- [48] Ewings, R. A. et al. Upgrade to the MAPS neutron time-of-flight chopper spectrometer. *Rev. Sci. Instrum.* **90**, 035110 (2019).
- [49] Lu, X. et al., Magnetic excitations of uniaxial-strain detwinned FeSe , STFC ISIS Neutron and Muon Source, <https://doi.org/10.5286/ISIS.E.RB2010578-1>